Global analysis of isospin dependent microscopic nucleon-nucleus optical potentials in a Dirac-Brueckner-Hartree-Fock approach

Ruirui Xu (续瑞瑞),* Zhongyu Ma (马中玉),† Yue Zhang (张玥), and Yuan Tian (田源)
China Institute of Atomic Energy, P.O. Box 275(41), Beijing 102413, China

E. N. E. van Dalen and H. Müther‡
Institut für Theoretische Physik, Universität Tübingen, Auf der Morgenstelle 14, D-72076 Tübingen, Germany
(Received 24 January 2016; revised manuscript received 7 August 2016; published 8 September 2016)

Background: For the study of exotic nuclei it is important to have an optical model potential that is reliable not only for stable nuclei but can also be extrapolated to nuclear systems with exotic numbers of protons and neutrons. An efficient way to obtain such a potential is to develop a microscopic optical potential (MOP) based on a fundamental theory with a minimal number of free parameters, which are adjusted to describe stable nuclei all over the nuclide chart.
Purpose: The choice adopted in the present work is to develop the MOP within a relativistic scheme which provides a natural and consistent relation between the spin-orbit part and the central part of the potential. The Dirac-Brueckner-Hartree-Fock (DBHF) approach provides such a microscopic relativistic scheme, which is based on a realistic nucleon-nucleon interaction and reproduces the saturation properties of symmetric nuclear matter without any adjustable parameter. Its solution using the projection technique within the subtracted T-matrix representation provides a reliable extension to asymmetric nuclear matter, which is important to describe the features of isospin asymmetric nuclei. The present work performs a global analysis of the isospin dependent nucleon-nucleus MOP based on the DBHF calculation in symmetric and asymmetric nuclear matter.
Methods: The DBHF approach is used to evaluate the relativistic structure of the nucleon self-energies in nuclear matter at various densities and asymmetries. The Schrödinger equivalent potentials of finite nuclei are derived from these Dirac components by a local density approximation (LDA). The density distributions of finite nuclei are taken from the Hartree-Fock-Bogoliubov approach with Gogny D1S force. An improved LDA approach (ILDA) is employed to get a better prediction of the scattering observables. A χ^2 assessment system based on the global simulated annealing algorithm is developed to optimize the very few free components in this study.
Results: The nucleon-nucleus scattering calculations are carried out for a broad spectrum of n and p scattering experiments below 200 MeV with targets ranging from ^{12}C to ^{208}Pb. The scattering observables including the neutron total cross section, proton reaction cross section, elastic scattering angular distribution, analyzing power, and spin rotation are evaluated and compared with the experimental data, as well as with results derived from the widely used phenomenological Koning-Delaroche global potential.
Conclusions: Results with the present relativistic MOP reproduce the $n, p + A$ scattering observables with good accuracy over a broad range of targets and a large region of energies fitting only the free-range factor t in ILDA and minor adjustments of the scalar and vector potentials in the low-density region.

DOI: 10.1103/PhysRevC.94.034606

I. INTRODUCTION

Nuclear reactions of unstable nuclei comprise a field of high interest of modern fundamental physics as well as applied nuclear physics. Experimental data about important parts of nuclear reaction chains, e.g., in nuclear reactors or astrophysical objects, are often sparse or lacking completely. Therefore, during the past few decades, considerable effort has been made to explore such nuclear reactions based on fundamental microscopic nuclear theories to obtain reliable predictions.

The optical model is a crucial component in such nuclear reaction studies, mainly because it determines the cross section for nuclear scattering and the formation of compound nuclei in the initial stage of a reaction and supplies the transmission coefficients for branching into the various final states [1]. Many observables such as the elastic scattering angular distribution, analyzing power, spin rotation function, and so on can be derived through the optical model. Therefore, the most important criteria to assess a microscopic optical potential (MOP) is that it can reproduce the existing experimental data of these observables as accurately as possible and make a reliable prediction without experimental guidance. Furthermore, the MOP is more appealing when it is established on better theoretical grounds with a small number of free parameters.

In the direct evaluation for MOP of finite nuclei attempts have been made to evaluate the scattering and absorption processes using a many-body theory for the target nuclei which goes beyond mean-field theory and incorporates, e.g., the effects of particle-vibration couplings. These studies typically

*xuruirui@ciae.ac.cn
†mazy12@ciae.ac.cn
‡herbert.muether@uni-tuebingen.de

employ an effective nucleon-nucleon (NN) interaction (e.g., Skyrme interaction or Gogny interaction). Recently, several investigations for finite nuclei have been reported [2,3]; however, it seems still infeasible to derive the MOP for all nuclei, which are of interest, e.g., in the field of applications of nuclear physics mentioned above. In addition, the investigation of the structure of target nuclei, especially for exotic nuclei, remains to be progressed. Using phenomenological NN interactions, such calculations are designed to derive the nuclear structure and the MOP from the same interaction model. A drawback of this scheme is that it is based on a phenomenological interaction fitted to describe structure data.

However, various attempts have been made to derive the MOP from a realistic model of the NN interaction, which means an interaction designed and fitted to describe the NN scattering data. Such studies often use the system of nuclear matter to determine the effects of correlations and evaluate the medium dependence of the resulting effective interaction for nuclear matter. The nuclear-matter results are then used in various kinds of local density approximation (LDA) to be applicable for finite nuclei. The review article of Ray *et al.* discusses various approximation schemes along this line [4].

Pioneering work along this line has been presented by Mahaux and co-workers [5], who evaluated the nucleon self-energy in nuclear matter as a function of density and energy in a Brueckner-Hartree-Fock (BHF) approximation and identified the resulting complex single-particle potential with the MOP for finite nuclei using LDA adopting nucleon density distributions from the empirical formula or microscopic nuclear structure calculations. One drawback of this scheme is that typically one has to use an interaction model for the evaluation of the density profile of the nuclei which is different from the realistic interaction used to calculate the self-energy in nuclear matter as BHF calculations fail to reproduce the empirical saturation properties for nuclear matter and finite nuclei. In a simplified way, some MOPs have been developed by adopting the effective NN interactions (e.g., Skyrme force) in the Hartree-Fock approach in nuclear matter and LDA for finite nuclei [6].

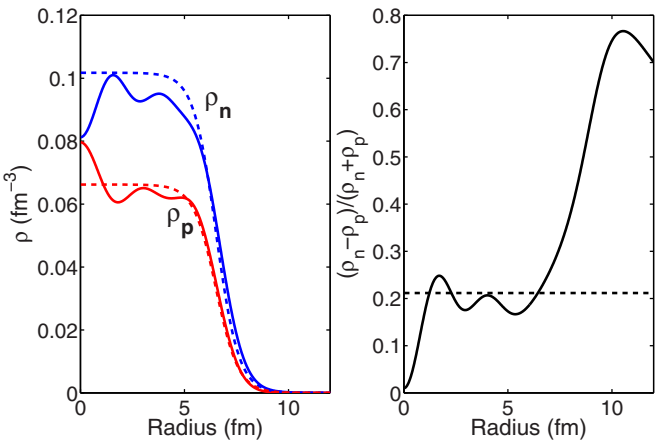

FIG. 1. The proton and neutron radial densities for ^{208}Pb. The solid and dashed lines indicate the calculated results from HFB and the Negele's empirical formula, respectively.

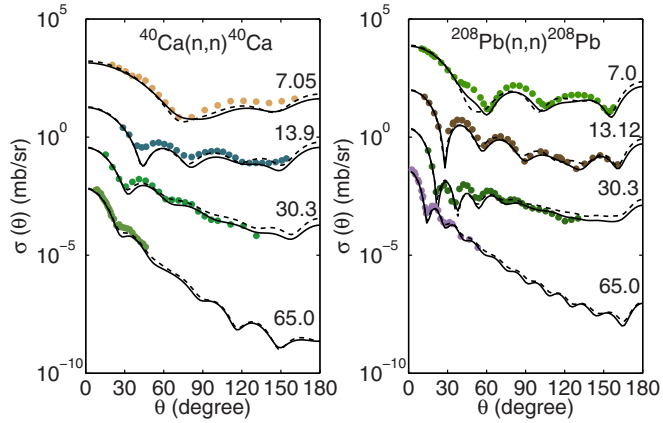

FIG. 2. Comparisons of angular distributions for $n + {}^{40}$Ca and ^{208}Pb at incident neutron energy around 7.0, 13.0, 30.0, and 65.0 MeV. The dashed line indicates the results based on a linear assumption of (f_1, f_2) and the solid line denotes the results with the values of (0.86,1.14), and the experimental data are listed in Table I.

Another handicap of this approach is the fact that this approach only provides the central part of the MOP; the spin-orbit potential has to be adjusted independently from the central potential in such a nonrelativistic approach. Nevertheless, this scheme was applied with quite some success by Jeukenne, Lejeune, and Mahaux already in the 1970s [5] and is still rather popular today.

Also the so-called g-folding method developed by Amos *et al.* [7] is based on a realistic NN interaction and uses a local density approximation to account for the medium dependence of the effective interaction. In this case, however, it is the NN interaction, which is evaluated by solving the Bethe-Goldstone

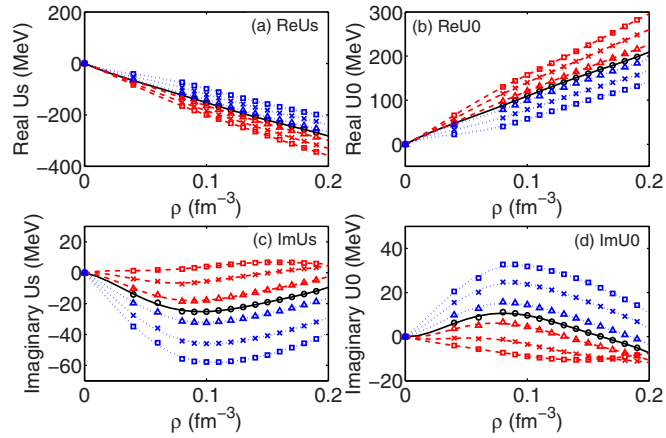

FIG. 3. Example for the real and imaginary part of the scalar (U_s) and vector (U_0) components of the Dirac potential as a function of density for nucleons with an incident particle energy of 90 MeV. The circles, triangles, x marks, and squares represent the calculated (adjusted) values for isospin asymmetries $\beta = 0.0$, 0.2, 0.6, and 1.0, respectively. The connecting solid line shows the polynomial interpolation in the case of symmetric matter, while the dashed and dotted lines visualize the corresponding interpolations for the neutron- and proton-potentials, respectively.

TABLE I. The $d\sigma/d\Omega$ database for neutron elastic scattering.

Target	Author (first)	Year	Energy (MeV)	Author (first)	Year	Energy (MeV)
6-C-12	R. O. Lane	1961	1.04, 2.25	P. Boschung	1971	4.04
	R. M. White	1980	6.94	G. Haouat	1975	8.5, 9.0
	D. W. Glasgow	1976	10.69, 12.49, 13.94	N. Olsson	1988	17.6, 22.0,
	T. Niizeki	1990	35.0	J. H. Osborne	2004	65.0, 107.5, 155, 225
	M. Ibaraki	2002	75.0	P. Mermod	2006	94.8
7-N-14	J. L. Fowler	1955	1.08, 1.68, 2.07	F. G. Perey	1974	4.34, 4.92, 6.01, 7.03, 8.56
	J. Chardine	1986	7.9, 9.0, 13.5	D. Schmidt	2003	10.81, 12.79
	L. Anli	1989	14.0, 17.0	N. Olsson	1989	21.6
8-O-16	L. Drigo	1976	2.56	I. A. Korzh	1980	5
	G. Boerker	1988	6.37, 7.51, 9.01, 10.31, 13.61, 14.89	M. Baba	1988	14.1
	L. Anli	1989	17	J. P. Delaroche	1986	18.0, 26.0
	N. Olsson	1989	21.6	P. Mermod	2006	94.8
11-Na-23	W. E. Kinney	1976	0.55, 0.7, 1.0, 1.2, 1.4, 1.6, 1.7, 2.0	U. Fasoli	1969	1.51, 2.47, 4.04
	Th. Schweitzer	1978	3.4	R. E. Coles	1971	5.0
	F. G. Perey	1970	5.44, 6.37, 7.6, 8.52	P. Kuijper	1972	14.8
12-Mg-24	D. B. Thomson	1962	3.79	I. A. Korzh	1994	5.0, 6.0, 7.0
	W. E. Kinney	1970	7.55, 8.56	M. Adel-Fawzy	1985	8.0, 9.0, 10.0, 11.0, 12.0
	A. Virdis	1981	9.76, 14.8	A. Takahashi	1987	14.1
	N. Olsson	1987	21.6			
13-Al-27	R. L. Becker	1966	3.2	W. E. Kinney	1970	5.44, 6.44, 7.54, 8.56
	G. Dagge	1989	7.62	C. S. Whisnant	1984	10.87, 13.88, 16.9
	M. M. Nagadi	2003	15.4	J. S. Petler	1985	18,20, 22,25, 26.0
	A. Bratenahl	1950	84.0	G. L. Salmon	1960	96.0
	C. P. Van Zyl	1956	136.0			
14-Si-28	W. E. Kinney	1970	5.44, 6.37, 6.44, 7.55, 8.56	C. R. Howell	1988	7.96, 9.95, 11.94, 13.97, 16.92
	J. Rapaport	1977	11.0, 20.0, 25.0	R. Alarcon	1986	21.7
	M. Ibaraki	2002	55.0, 65.0, 75.0			
15-P-31	K. Tsukada	1961	3.5,3.8,4.2,4.5	J. Martin	1968	5.95
	J. D. Brandenberge	1972	7.79,9.05	P. H. Stelson	1965	14.0
	G. C. Bonazzola	1965	14.2			
16-S-32	F. G. Perey	1970	3,4, 7.05, 7.6, 8.52	S. Tanaka	1969	5.92
	C. R. Howell	1988	7.96, 9.95, 11.93, 13.92	J. D. Brandenberge	1972	9.05
	A. Virdis	1981	9.76	J. Rapaport	1977	20.0, 26.0
	Y. Yamanouti	1977	21.5	R. Alarcon	1986	21.7
	J. S. Winfield	1986	30.3, 40.3			
19-K-39	J. H. Towle	1965	1.49, 2.38	J. D. Reber	1967	2.06, 3.74, 4.33, 6.52, 7.91
	A. J. Frasca	1966	14.0			
20-Ca-40	J. D. Reber	1967	2.06, 3.29, 5.3, 7.91	B. Holmqvist	1969	6.09, 7.05
	W. Tornow	1982	9.91, 11.9, 13.9	G. M. Honore	1986	16.9
	R. Alarcon	1987	19.0, 25.5	J. Rapaport	1977	20.0
	N. Olsson	1987	21.6	R. P. Devito	1981	30.3
	E. L. Hjort	1994	65.0	J. H. Osborne	2004	107.5, 185.0
22-Ti-48	A. B. Smith	1998	4.5, 5.5, 6.5, 7.55, 8.08, 8.41, 9.06, 9.5, 9.99	C. St. Pierre	1959	14.0
24-Cr-52	B. Holmqvist	1969	3,4	W. E. Kinney	1974	4.34, 4.92, 6.44, 8.56
	A. B. Smith	1997	7.52	D. Schmidt	1998	7.95, 9.0, 9.8, 10.79, 11.44, 12.01, 12.7, 13.65, 14.1, 14.76
	N. Olsson	1987	21.6			
25-Mn-55	B. Holmqvist	1969	2.47, 3.0, 3.49, 4.0, 4.56, 6.09, 7.05, 8.05	Th. Schweitzer	1978	3.4
	A. Takahashi	1992	14.1			
26-Fe-56	V. M. Morozov	1972	1.8	W. E. Kinney	1968	4.6, 5.0, 5.56, 6.12, 6.53, 7.55
	P. Boschung	1971	5.05	Ruan Xichao	2009	8.17
	S. Mellema	1983	11.0, 20, 26	N. Olsson	1987	21.6
	T. P. Stuart	1962	24.8	M. Ibaraki	2002	55.0, 65.0, 75.0

TABLE I. *(Continued.)*

Target	Author (first)	Year	Energy (MeV)	Author (first)	Year	Energy (MeV)
27-Co-59	B. Holmqvist	1969	1.46, 2.0, 2.47, 3.0, 3.49, 4.0, 4.56, 6.09, 7.05, 8.05	M. M. Nagadi	2003	9.95, 15.43, 16.88, 18.86
	L. F. Hansen	1985	14.6	N. Olsson	1987	21.6
	S. T. Lam	1985	23.0			
28-Ni-58	B. Holmqvist	1969	3.0	W. E. Kinney	1974	4.34, 6.44, 7.54, 8.56
	A. B. Smith	1992	5.5, 6.5, 8.4, 9.5, 9.99	P. P. Guss	1985	7.9, 9.96, 13.94
	E. G. Christodoulo	1999	14.0	A. Takahashi	1992	14.1
	R. S. Pedroni	1988	16.9	N. Olsson	1987	21.6
	Y. Yamanouti	1979	24.0			

equation in nuclear matter and then employed in a folding calculation to evaluate the MOP for finite nuclei. The g-folding approach has very successfully been applied to reproduce differential cross sections and spin observables for many nuclei from ^{6}Li to ^{238}U without adjustable parameters [7–14].

The Mahaux scheme as well as the g-folding method are based on a nonrelativistic (NR) approach and the energy dependence of the MOP originates from the energy dependence of the effective interaction g calculated for nuclear matter in a nonrelativistic Brueckner-Hartree-Fock approximation. Also the work presented in this paper is based on a realistic model of the NN interaction and accounts for the effects of correlations presented in the g matrix. In contrast to the nonrelativistic approaches, however, it takes the relativistic structure of the nucleon spinors into account.

An alternative approach is based on the Dirac phenomenology as it has been introduced by Walecka and co-workers [15]. Within this Dirac phenomenology the nucleon self-energy contains a large and attractive component, which transforms like a scalar under a Lorentz transformation compensated to a large extent by a repulsive Lorentz vector component. If one reduces the corresponding Dirac equation for the nucleon in the nuclear-matter medium to a nonrelativistic Schrödinger equation, one obtains a Schrödinger equivalent potential with a central potential which is energy dependent and a strong spin-orbit term.

An application of this Dirac phenomenology to describe the optical model potential has been presented by Cooper *et al.* [16]. They developed a phenomenological parametrization of the real and imaginary parts of the scalar and vector potentials. Fitting the corresponding parameters, which depend on energy and mass number of the target nucleus, they obtain a very good global fit of the optical model potential.

A comparison of the rather successful but very different approaches to a global optical potential, the g-folding method and Dirac phenomenology, has been made by Deb *et al.* [11]. They evaluated differential cross sections and spin observables for nucleon nucleus scattering on five different targets ranging from ^{12}C to ^{208}Pb at energies of 65 and 200 MeV using both approaches and conclude that the results are of similar quality.

It is one aim of the Dirac-Brueckner-Hartree-Fock approach (DBHF) approach to combine the features of a realistic NN interaction and its dependence on the medium, as they are contained in the Mahaux approach and the g-folding model with those of the Dirac phenomenology [17]. This approach is founded on a realistic NN interaction and the treatment of nuclear correlations and the medium dependence of the effective NN interaction is done in straight analogy to the Mahaux approach and the g-folding method. The DBHF approach, however, keeps track of the relativistic structure of the nucleon self-energy and therefore one can determine the real and the imaginary parts of the scalar and vector component of the nucleon self-energy in nuclear matter as a function of momentum, density, and energy. These components are then used to evaluate the corresponding MOP using LDA for these components of the self-energy in straight analogy to the Mahaux scheme.

In this way, the spin-orbit potential arises naturally from the coherent sum of the contribution from the scalar and vector potentials in this relativistic scheme, and the saturation properties of symmetric nuclear matter are reproduced in the relativistic DBHF approach, while three-nucleon forces have to be introduced to obtain a corresponding result within the nonrelativistic BHF approximation [18–20]. Therefore, it seems rather attractive to determine a microscopic optical model based on the DBHF approach as, finally, one may be able to describe the ground-state properties of nuclei and the MOP within the same theoretical framework.

For a long period it has been a challenge in theoretical nuclear physics to solve the Brueckner-Hartree-Fock scheme in the relativistic way, especially for isospin asymmetric nuclear matter. In recent years substantial progress has been obtained using a so-called subtracted T matrix (STM) representation in the projection technique to solve DBHF scheme strictly in the symmetric and asymmetric nuclear matter [21].

In a preliminary study we have explored the isospin dependent relativistic microscopic optical potential adopting the self-energies from this DBHF calculation in Ref. [17]. This MOP has been verified by satisfactorily reproducing the neutron and proton scattering data from ^{27}Al. In this work, a systematic investigation for this MOP is performed in a large range of nuclei. The microscopic radial nucleon density of finite nuclei based on the Hartree-Fock-Bogoliubov (HFB) calculation are adopted in this calculation instead of the previous empirical values. Meanwhile, a χ^2 assessment system based on the global simulated annealing algorithm (GSA) is specially designed to optimize the free factors and give an overall estimation on the performance of this MOP.

TABLE II. The $d\sigma/d\Omega$ database for neutron elastic scattering.

Target	Author (first)	Year	Energy (MeV)	Author (first)	Year	Energy (MeV)
29-Cu-63	P. Guenther	1986	1.6, 2,3, 3.9	W. E. Kinney	1974	5.5, 7.0, 8.5
	S. M. El-Kadi	1982	7.96, 9.94, 11.93, 13.92	J. D. Anderson	1959	14.6
	B. Ya. Guzhovskiy	1961	15.0	A. Begum	1979	16.1
	A. Bratenahl	1950	84.0	G. L. Salmon	1960	96.0
	C. P. Van Zyl	1956	136.0			
34-Se-80	R. M. Musaelyan	1987	0.34	E. S. Konobeevskij	1984	1.19
	I. A. Korzh	1983	1.5, 2.0, 2.5, 3,5	G. V. Gorlov	1964	4
	R. G .Kurup	1984	8.0, 10.0			
38-Sr-88	S. A. Cox	1972	0.886	M. Walt	1954	1
	D. W. Kent	1962	3.66	V. I. Popov	1971	4.37
	D. E. Bainum	1978	11			
39-Y-89	R. D. Lawson	1986	4.5, 5.0, 5.5, 5.9, 6.5, 7.14, 7.5, 8.03, 8.4, 9.06, 9.5, 9.99	F. G. Perey	1970	7.6, 8.56
	G. M. Honore	1986	7.96, 9.95, 11.94, 13.93	S. Mellema	1987	11.0
	N. Olsson	1987	21.6			
40-Zr-90	P. Guenther	1975	2.0, 2.2, 2.6, 3,4	R. W. Stooksberry	1976	2.11
	S. Chiba	1992	4.5, 5.0, 5.5, 5.9, 6.5, 8.03, 9.06, 9.99	Y. Wang	1990	10.0, 24.0
	D. E. Bainum	1978	11.0	M. Ibaraki	2002	55.0, 65.0, 75.0
41-Nb-93	A. B. Smith	1985	4.5, 5.0, 5.5, 5.9, 6.5, 7.14 7.5, 8.03, 8.4, 9.06	R. S. Pedroni	1991	7.95, 9.94, 11.93, 13.92, 16.91
	J. C. Ferrer	1977	11.0	E. G. Christodoulo	1999	14.0
	R. Finlay	1991	20.0			
42-Mo-98	P. Lambropoulos	1973	1.5	A. B. Smith	1975	2.0, 3.0, 4.0
	J. Rapaport	1979	7.0, 9.0, 11.0, 16.0, 20.0, 26.0			
45-Rh-103	A. B. Smith	1994	4.51, 5.0, 5.9, 6.5, 7.5, 8.03, 8.4, 9.06, 9.5, 10.0			
49-In-115	S. A. Cox	1972	0.87	B. Holmqvist	1969	3.0, 4.0, 7.05, 8.05
	A. B. Smith	1984	3.05, 3.75	R. L. Becker	1966	3.2
	S. Chiba	1990	4.5, 5.0, 5.9, 7.14, 8.03, 9.06, 9.99	J. C. Ferrer	1977	11.0
	J. O. Elliot	1956	14.0	L. F. Hansen	1985	14.6
50-Sn-120	S. Tanaka	1972	1.52, 2.05, 2.57, 3.08	C. Budtz-Jorgense	1984	3.0, 3.2, 3.4, 3.6, 3.8, 4.0
	R. M. Wilenzick	1965	6.04	P. P. Guss	1989	9.94, 13.92, 16.91
	J. Rapaport	1980	11.0	T. P. Stuart	1962	24.0
	E. L. Hjort	1994	65.0			
79-Au-197	R. B. Day	1965	0.5, 2.5	F. T. Kuchnir	1968	0.6, 1.6
	S. A. Cox	1972	0.878, 2.0	A. B. Smith	2005	4.51, 5.51, 6.51, 7.51, 8.41, 9.99
	S. C. Buccino	1966	5	M. A. Etemad	1973	7
	B. Holmqvist	1971	8.05	L. F. Hansen	1985	14.6
82-Pb-208	V. M. Morozov	1972	1.8	J. R. M. Annand	1985	4.0, 5.0, 6,7
	D. Schmidt	1996	7.93, 8.98, 9.87, 10.96, 11.92, 13.12, 14.23	W. E. Kinney	1974	8.5
	J. Rapaport	1978	11.0, 26.0	A. Takahashi	1987	14.1
	R. W. Finlay	1984	20.0, 22.0, 24.0	R. P. Devito	1980	30.3, 40.0
	M. Ibaraki	2002	55, 65.0, 75.0	A. Bratenahl	1950	84.0
	J. H.Osborne	2004	85.0, 95.0, 107.0, 127.5, 155.0, 185.0, 225.0	A. Oehrn	2008	96.0
	C. P. Van Zyl	1956	136.0			
83-Bi-209	N. Olsson	1982	1.48, 1.97, 2.23, 3.05	J. R. M. Annand	1985	4.0, 5.0, 5.5, 6.5, 7.0
	R. K. Das	1990	7.5, 8.0, 9.0, 10.0, 11.0, 12.0, 20.0, 24.0	N. Olsson	1987	21.6

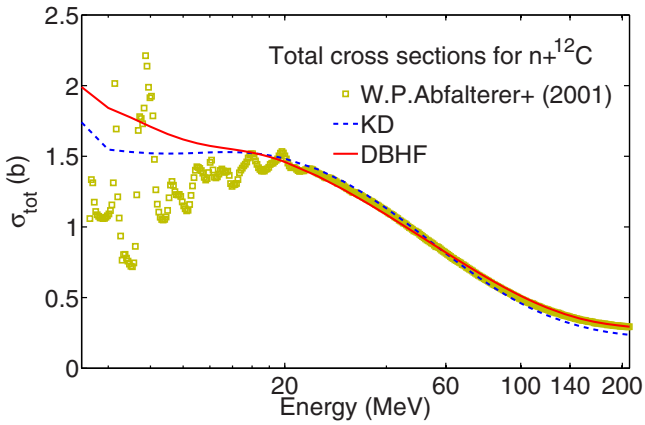

FIG. 4. Comparison of predicted neutron total cross section (solid line) and experimental data (points) and KD calculation (dashed line) for $n + {}^{12}$C. The experimental data are measured for natural carbon.

The paper is composed as follows. In Sec. II, the general formalism of the DBHF approach is briefly introduced. The isospin dependent relativistic MOPs of finite nuclei are built in Sec. III through combining the self-energies and the microscopic radial nucleon density by the improved local density approximation (ILDA) [5]. The global analysis of nuclear scattering is carried out in Sec. IV for neutron and proton scattering and induced reactions on ^{12}C-^{208}Pb and the calculated results are compared with the calculated results with the widely used phenomenological Koning-Delaroche (KD) global optical potential [22] and the experimental data of various scattering quantities. Finally, the overall discussion is summarized in Sec. V.

II. SELF-ENERGY IN NUCLEAR MATTER

Realistic NN interactions contain strong short-range and tensor components. Therefore, it is necessary to account for the corresponding correlations between the interacting nucleons. In the relativistic Brueckner-Hartree-Fock approach this is achieved by considering the equation for two interacting nucleons in nuclear matter. This leads to the ladder approximation of the relativistic Bethe-Salpeter (BS) equation [21,23], written in an abbreviated operator notation,

$$T = V + VQGGT, \tag{1}$$

where T is the nucleon-nucleon interaction matrix in the nuclear medium and V is the bare NN interaction, respectively. The Pauli exclusion principle is included by the Q operator and the in-medium nucleon propagation of the nucleons is described by the Green's function G. Therefore, GG represents the two-nucleon propagator in nuclear matter. The Green's function G fulfills the Dyson equation,

$$G = G_0 + G_0 \Sigma G. \tag{2}$$

G_0 denotes the free nucleon propagator, and the self-energy term Σ is defined in first order of the effective interaction T

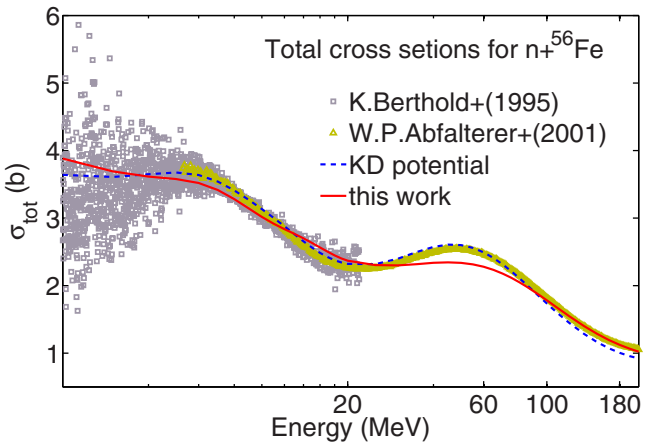

FIG. 5. Comparison of predicted neutron total cross section (solid line) and experimental data (points) and KD calculation (dashed line) for $n + {}^{56}$Fe. The experimental data are measured for natural iron.

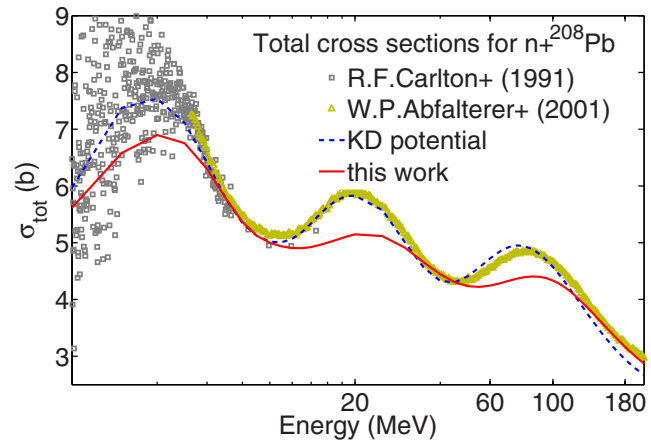

FIG. 6. Comparison of predicted neutron total cross section (solid line) and experimental data (points) and KD calculation (dashed line) for $n + {}^{208}$Pb. The experimental data are measured for natural lead.

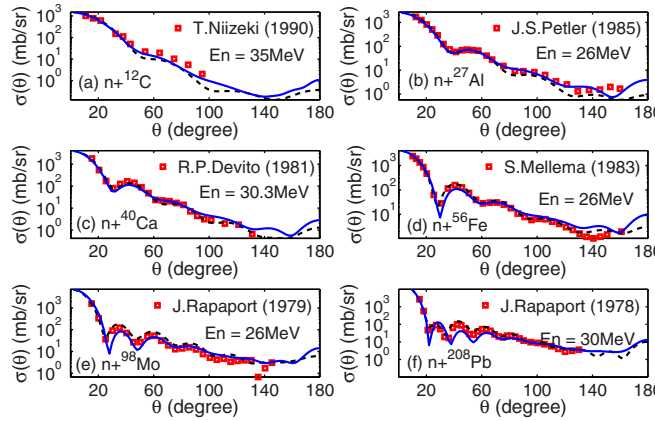

FIG. 7. Comparisons of angular distributions for $n + {}^{12}$C, ^{27}Al, ^{40}Ca, ^{56}Fe, ^{98}Mo, and ^{208}Pb at incident neutron energy around 30 MeV. The dashed lines indicate the results from KD potential and the solid lines denote the present prediction.

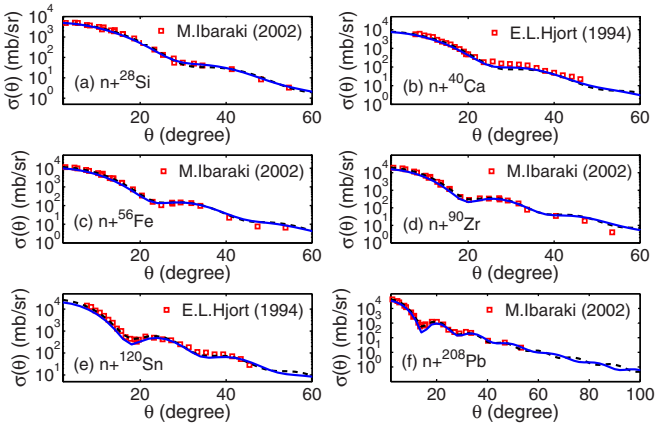

FIG. 8. Comparisons of angular distributions for $n + {}^{28}$Si, ^{40}Ca, ^{56}Fe, ^{90}Zr, ^{120}Sn, and ^{208}Pb at incident neutron energy around 65 MeV. The dashed line indicates the results from KD potential and the solid line denotes the present prediction.

through the following standard Hartree-Fock equation

$$\Sigma = \mathrm{Tr}[GT]. \tag{3}$$

Note that the self-energy contains the direct and exchange terms at the same time, and the Tr symbol denotes a trace on spin and isospin quantum numbers as well as a momentum integration over all nucleon within the Fermi sea. Because Eqs. (1)–(3) are strongly coupled, they have to be solved iteratively until convergence is reached.

Generally, the Lorentz structure of the relativistic self-energy Σ can be expressed as [24]

$$\Sigma^m(k,k_F,\beta) = \Sigma_s^m(k,k_F,\beta) - \gamma_0\Sigma_0^m(k,k_F,\beta) + \boldsymbol{\gamma}\cdot\mathbf{k}\Sigma_v^m(k,k_F,\beta). \tag{4}$$

In this equation, Σ_s is the scalar part of self-energy and Σ_0 and Σ_v denote the timelike and spacelike terms of the vector part, respectively. The superscript m is used to sign the proton and neutron because they should be distinguished in isospin asymmetric nuclear matter. Note that these components of the self-energy are functions of the nucleon momentum (k),

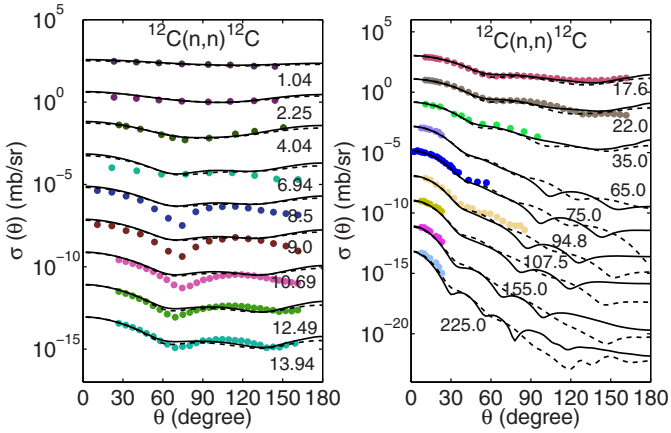

FIG. 9. Comparison of predicted $d\sigma/d\Omega$ (solid lines) and experimental data (points) and KD calculation (dashed lines) for $n + {}^{12}$C.

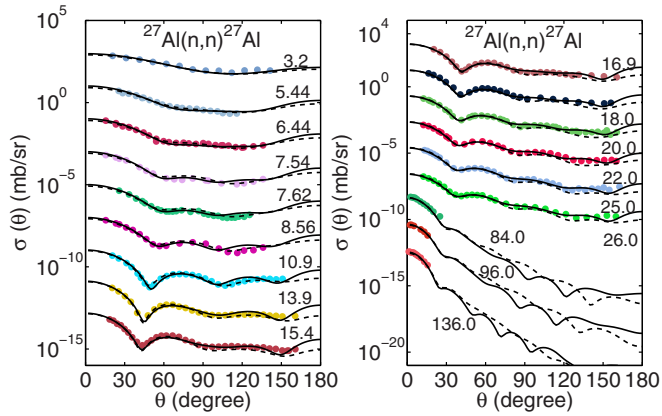

FIG. 10. Comparison of predicted $d\sigma/d\Omega$ (solid lines) and experimental data (points) and KD calculation (dashed lines) for $n + {}^{27}$Al.

density or Fermi momentum (k_F), and asymmetry parameter $\beta = (\rho_n - \rho_p)/\rho$, where ρ_n, ρ_p, and ρ indicate the neutron, proton, and total densities in nuclear matter, respectively.

Details of such DBHF calculations and the method to extract these Dirac components using the STM representation are described in Refs. [21,25,26]. The self-energies used in the present study are determined using the Bonn B potential [27] for the bare NN interaction and solving the DBHF equations for isospin asymmetric nuclear matter with various densities and isospin asymmetries.

III. RELATIVISTIC MICROSCOPIC OPTICAL POTENTIAL IN FINITE NUCLEI

In the relativistic scheme, the wave function of an incident particle described in terms of a Dirac spinor Ψ is obtained by the solution of the corresponding Dirac equation,

$$\left[\vec{\alpha}\cdot\vec{p} + \gamma_0(M + U_s^m) + U_0^m\right]\Psi^m = \varepsilon\Psi^m, \tag{5}$$

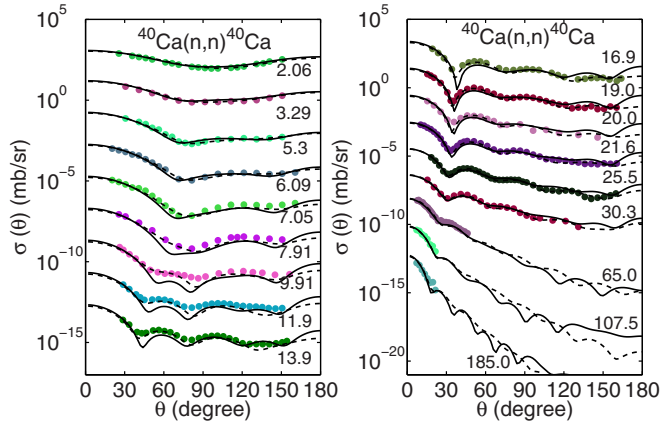

FIG. 11. Comparison of predicted $d\sigma/d\Omega$ (solid lines) and experimental data (points) and KD calculation (dashed lines) for $n + {}^{40}$Ca.

TABLE III. The χ^2/N of $d\sigma/d\Omega$ for $n + {}^{12}\mathrm{C}$ -${}^{40}\mathrm{Ca}$ reactions.

Nuclide	N of data points	MOP	KD
${}^{12}\mathrm{C}$	293	3.35	2.43
${}^{14}\mathrm{N}$	336	0.21	0.22
${}^{16}\mathrm{O}$	309	0.91	0.66
${}^{23}\mathrm{Na}$	221	0.31	0.22
${}^{24}\mathrm{Mg}$	270	0.56	0.19
${}^{27}\mathrm{Al}$	426	0.068	0.069
${}^{28}\mathrm{Si}$	391	0.24	0.15
${}^{32}\mathrm{S}$	388	0.22	0.07
${}^{40}\mathrm{Ca}$	399	0.22	0.075

where U_s^m and U_0^m are the scalar and vector components of the scattering potential,

$$U_s^m = \frac{\Sigma_s^m - \Sigma_v^m M}{1 + \Sigma_v^m}, \quad U_0^m = \frac{-\Sigma_0^m + \varepsilon \Sigma_v^m}{1 + \Sigma_v^m}, \tag{6}$$

and $\varepsilon = E + M$ is the single-particle energy, E is the kinetic energy of the nucleon in the free space, and M indicates the mass of the nucleon.

To calculate the scattering observables of finite nuclei, this Dirac equation is typically reduced to a Schrödinger-type equation by eliminating the lower components of the Dirac spinor in a standard way. The equation for the upper components of the wave function is transformed into

$$\left[-\frac{\nabla^2}{2\varepsilon} + V_{\mathrm{cent}}^m + V_{\mathrm{s.o.}}^m(r)\vec{\sigma} \cdot \vec{\mathrm{L}} + V_{\mathrm{Darwin}}^m(r) \right] \varphi(\mathbf{r}) = \frac{\varepsilon^2 - M^2}{2\varepsilon} \varphi(\mathbf{r}), \tag{7}$$

where V_{cent}^m, $V_{\mathrm{s.o.}}^m$, and V_{Darwin}^m represent the Schrödinger equivalent central, spin-orbit, and Darwin potentials, respectively. The potentials in Eq. (8) are obtained from the scalar U_s and vector U_0 potentials as

$$\begin{aligned} V_{\mathrm{cent}}^m &= \frac{M}{\varepsilon} U_s^m + U_0^m + \frac{1}{2\varepsilon}[U_s^{m2} - (U_0^m + V_c)^2], \\ V_{\mathrm{s.o.}}^m &= -\frac{1}{2\varepsilon r D^m(r)} \frac{dD^m(r)}{dr}, \\ V_{\mathrm{Darwin}}^m &= \frac{3}{8\varepsilon D^m(r)} \left[\frac{dD^m(r)}{dr} \right]^2 - \frac{1}{2\varepsilon r D^m(r)} \frac{dD^m}{dr} \\ &\quad - \frac{1}{4\varepsilon D^m(r)} \frac{d^2 D^m(r)}{d^2 r}, \end{aligned} \tag{8}$$

TABLE IV. The χ^2/N of $d\sigma/d\Omega$ for $n + {}^{48}\mathrm{Ti}$ -${}^{63}\mathrm{Cu}$ reactions.

Nuclide	N of data points	MOP	KD
${}^{48}\mathrm{Ti}$	378	0.13	0.05
${}^{52}\mathrm{Cr}$	562	0.16	0.03
${}^{56}\mathrm{Fe}$	333	0.23	0.09
${}^{58}\mathrm{Ni}$	701	0.17	0.11
${}^{63}\mathrm{Cu}$	282	0.11	0.06

TABLE V. The χ^2/N of $d\sigma/d\Omega$ for $n + {}^{80}\mathrm{Se}$ -${}^{209}\mathrm{Bi}$ reactions.

Nuclide	N of data points	MOP	KD
${}^{80}\mathrm{Se}$	152	0.17	0.11
${}^{88}\mathrm{Sr}$	81	0.09	0.03
${}^{89}\mathrm{Y}$	620	0.19	0.05
${}^{90}\mathrm{Zr}$	1110	0.14	0.05
${}^{93}\mathrm{Nb}$	629	0.13	0.03
${}^{98}\mathrm{Mo}$	180	0.30	0.36
${}^{103}\mathrm{Rh}$	400	0.12	0.06
${}^{115}\mathrm{In}$	744	0.10	0.05
${}^{120}\mathrm{Sn}$	357	0.08	0.03
${}^{140}\mathrm{Ce}$	105	0.19	0.05
${}^{197}\mathrm{Au}$	390	0.22	0.10
${}^{208}\mathrm{Pb}$	885	2.25	1.80
${}^{209}\mathrm{Bi}$	767	0.27	0.06

where V_c is the Coulomb potential for a charged particle and D denotes a quantity defined as

$$D^m(r) = M + \varepsilon + U_s^m(r) - U_0^m(r) - V_c. \tag{9}$$

The radial potentials in finite nuclei, namely, V_{cent}^m, $V_{\mathrm{s.o.}}^m$, and V_{Darwin}^m in Eqs. (8) and (9), can be associated with the scalar U_s and vector U_0 in nuclear matter through the LDA using the local nucleon density $\rho(r)$ for the nucleus considered. In this work, a finite range correction in Gaussian form is adopted in LDA to further remedy the potentials to obtain the better prediction of the scattering experimental data, that is, the so-called ILDA,

$$U_{\mathrm{ILDA}}(r,E) = (t\sqrt{\pi})^{-3} \int U_{\mathrm{LDA}}(r',E) \exp(-|\vec{r} - \vec{r'}|^2/t^2) d^3r', \tag{10}$$

where t is an effective range parameter of the potential U_{LDA} in normal LDA approach at radius r' [5,17]. It is included to account for a finite-range correction of the nucleon-nucleon interaction, which is not incorporated in the DBHF calculation. They modify the radial distribution of $\mathrm{V_{cent}}$ while keeping its volume integral constant. The potential U_{LDA} is related to the U_s and U_0 in nuclear matter by

$$U_{\mathrm{LDA}}(r,E) = U_{\mathrm{NM}}(k, E, \rho(r), \beta(r)), \tag{11}$$

and U_{NM} represent the corresponding potential in nuclear matter using the isospin asymmetry β of the target nucleus and the momentum k and energy E of the incoming nucleon. In our present studies we adopt the radial nucleon density, $\rho(r)$, from the HFB approach with Gogny D1S force [28], instead of the empirical values by the Negele's formula [29], which has been employed for our pilot study [17].

In Fig. 1, we compare the radial density and asymmetry distributions for ${}^{208}\mathrm{Pb}$ as derived from HFB approach and the empirical formula. The radial densities obtained in the HFB approach show oscillations in the interior of the nucleus, which reflect the structure of the single-particle wave functions. Note, however, that the oscillations are smoothed out to a large extent in the ILDA potentials by the finite range correction of Eq. (10). Also note the enhancement of the neutron density in the surface

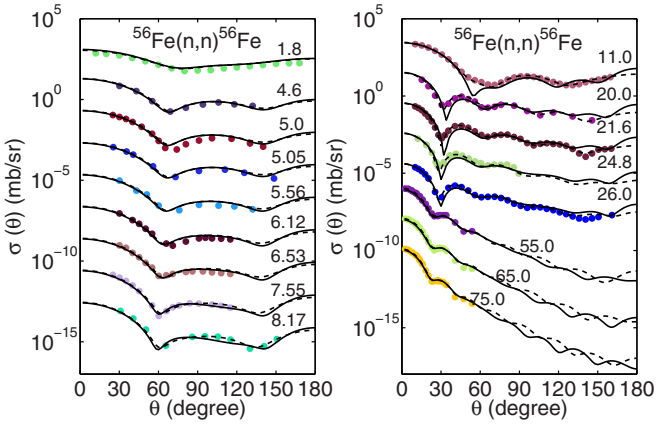

FIG. 12. Comparison of predicted $d\sigma/d\Omega$ (solid lines) and experimental data (points) and KD calculation (dashed lines) for $n + {}^{56}$Fe.

of the nucleus in the microscopic calculation. This neutron skin leads to large isospin asymmetries, as presented in the left panel of Fig. 1.

In addition, as for this microscopic optical potential, the applicability of the theory should indicate that the formalism does not include the coupling to giant resonances (10 to 30 MeV) and the compound nucleus formation (< 10 MeV), which has been discussed before and stressed in, e.g., Ref. [7]. At the low energies, we include the compound nuclear contribution to the elastic differential cross sections by the Hauser-Feshbach statistic theory through the optical model code APMN [30], which employs the Hauser-Feshbach model to determine the contributions from the compound nuclear elastic scattering by concerning six competing single-particle emission reactions, including neutron, proton, deuteron, tritium, α, and ^{3}He. The formation of giant resonances will be discussed further in other future work.

IV. GLOBAL ANALYSIS OF NUCLEON-NUCLEI RELATIVISTIC MICROSCOPIC OPTICAL POTENTIAL

A. Dirac potentials in the *full* density region for finite nuclei

Most experimental data have been taken for stable nuclei and very limited scattering data exist for unstable isotopes. Therefore, the eventual goal of this work is to develop a relativistic MOP model which is capable of describing scattering data for all stable nuclei and will be tested for many unstable nuclei in the near future. The microscopic basis of the present calculations originates from the real and imaginary parts of the Dirac components, U_s^m and U_0^m, of the nucleon self-energies calculated in the DBHF approach for symmetric and asymmetric nuclear matter. Such DBHF calculations, however, yield reliable results only for densities $\rho > 0.08\,\mathrm{fm}^{-3}$. The procedure to derive self-consistent DBHF results does typically not converge at lower densities. This reflects the situation that homogeneous nuclear matter is unstable at such low densities with respect to the formation of an inhomogeneous density profile containing nuclear clusters. In particular, the solution of the T matrix of Eq. (1) yields bound states in the deuteron channel.

For the derivation of the optical model potential for finite nuclei, however, we also need results at densities $\rho < 0.08\,\mathrm{fm}^{-3}$. Therefore, we have to extrapolate the results to these low densities with the natural constraint that the Dirac potentials U_s^m and U_0^m vanish at $\rho = 0$. As a first guess for these data points below $\rho = 0.08\ \mathrm{fm}^{-3}$ one may take a linear extrapolation, which would be too simple. To make the extrapolation process more flexible, we introduce auxiliary mesh points at $\rho = 0.04\ \mathrm{fm}^{-3}$ for the real parts and at $\rho = 0.04$ and $0.06\ \mathrm{fm}^{-3}$ for the imaginary parts, and the "initial" values of U_s^m and U_0^m at these points are obtained using linear assumption. Then, two enhancement factors are involved to slightly modify the initial values (f_1 for the real U_s^m and U_0^m, f_2 for the imaginary U_s^m and U_0^m) to achieve the "optimized" values. Based on the optimized values and the microscopic results by DBHF at $\rho > 0.08\,\mathrm{fm}^{-3}$, the polynomial fittings are employed to derive the Dirac potentials in the *full* density space to construct the Schrödinger equivalent potentials of finite nuclei. In practice, we have chosen to represent the density dependence of the Dirac potentials in terms of a polynomial fit with a polynomial of degree 5 for the real part and a polynomial of degree 7 for the imaginary part. Actually, a large amount of such polynomial fittings are required one by one corresponding to all incident nucleon energies and isospin asymmetries of finite nuclei in this study. The central issue in the whole process is to fix the values of (f_1, f_2), and they are expected to be constant for all cases to minimize phenomenological effect. A χ^2 assessment system is specially designed to fulfill this optimization, which is illuminated as follows. In addition, the effective range factor t in Eq. (10) is also fixed in company with (f_1, f_2) in the same process.

First of all, as mentioned in Sec. I, one of the main criteria to evaluate a good optical model potential is that it can well reproduce as many of the measured scattering observables as possible. Therefore, we utilize the experimental scattering data in the χ^2 assessment. ^{40}Ca and ^{208}Pb, for which a large number of experimental data of proton and neutron scattering were measured, are both double-magic nuclei and they represent proper examples to cover a good range from isospin symmetric

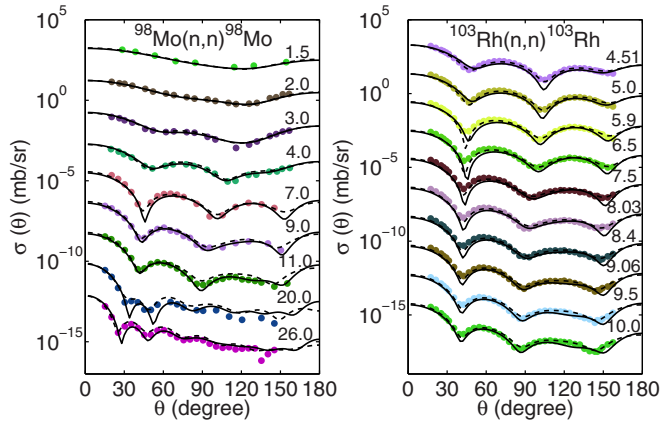

FIG. 13. Comparison of predicted $d\sigma/d\Omega$ (solid lines) and experimental data (points) and KD calculation (dashed lines) for $n + {}^{98}$Mo and ^{103}Rh.

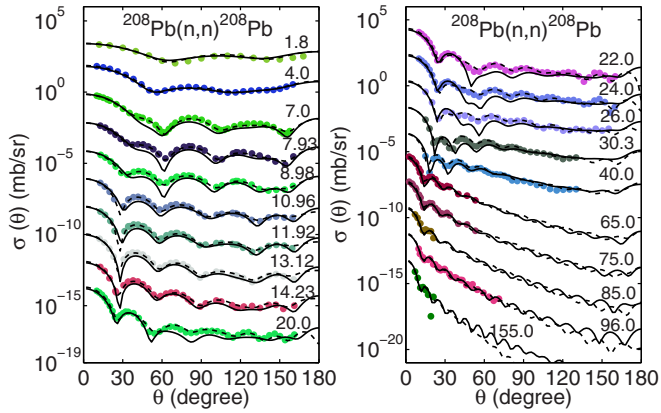

FIG. 14. Comparison of predicted $d\sigma/d\Omega$ (solid lines) and experimental data (points) and KD calculation (dashed lines) for $n + {}^{208}$Pb.

to asymmetric nuclei; consequently, the scattering data of these two nuclei were selected for optimization in this study.

Most optimization procedures obtain the parameters through minimizing a certain χ^2 value [22,31], given, for example, by

$$\chi^2 = \sum_{i=1}^{P} \left(\frac{\sigma_i^{\rm cal} - \sigma_i^{\rm exp}}{\sigma_i^{\rm exp}} \right)^2, \qquad (12)$$

where $\sigma_i^{\rm exp}$ is the ith experimental point, $\sigma_i^{\rm cal}$ is the ith calculated result, and P indicates the total number of experimental data in the consideration. In this work, the value of χ^2/N is adopted as the criteria for optimization. χ^2 uses the same form with Eq. (12), $N = P - F$ is the number of degrees of freedom, and F is the number of free parameters. Meanwhile, we employ the GSA method based on the Monte Carlo sampling in a predefined region of the free parameters to search the minimal χ^2/N. It is known, however, that it is not possible to obtain a "best fit" through the numerical optimization procedure alone [22]; therefore, a visual goodness-of-fit

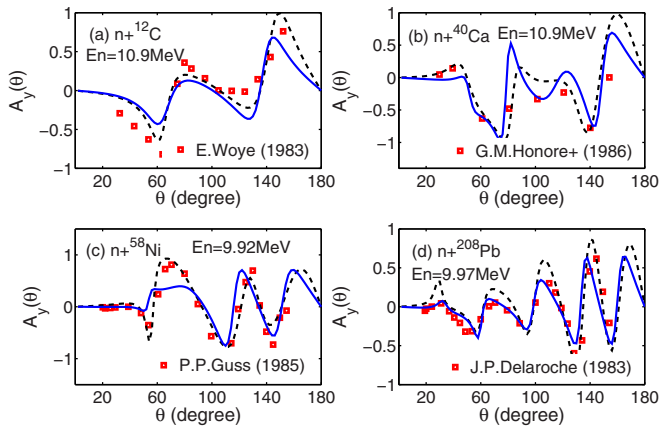

FIG. 15. Comparisons of analyzing power for $n + {}^{12}$C, ^{40}Ca, ^{58}Ni, and ^{208}Pb at incident neutron energy around 10 MeV. The dashed line indicates the results from KD potential and the solid line denotes the present work.

estimation evaluator is also incorporated. In this work, in a first step the angular distributions of elastic scattering, $d\sigma/d\Omega$, of ^{40}Ca and ^{208}Pb are taken into account to optimize the χ^2/N between experimental data and our theoretical calculations. After the "minimal" χ^2/N value is achieved for $d\sigma/d\Omega$, the other observables, such as analyzing power (A_y) for nucleon-nucleus elastic scattering as well as the neutron total cross section ($\sigma_{\rm tot}$) and proton total reaction cross section ($\sigma_{\rm reac}$), etc., are then utilized in the visual goodness estimation for a further assessment of MOP.

As a result, (f_1, f_2) is searched as (0.86,1.14), which is slightly different from an absolute linear shape with $(f_1, f_2) = (1.0, 1.0)$, and the effect range factor t is determined as 1.35 fm for p-A and 1.45 fm for n-A, which are comparable to $t = 1.4$ fm derived in our pilot study [17] focused on the target nucleus ^{27}Al. Moreover, it is found that the calculation of MOP are not very sensitive to variations of f_1 and f_2. Both the linear assumption and the optimized one can provide a good reproduction to scattering observables, as illuminated in Fig. 2. However, the χ^2/N value is improved a little; for example, the value is changed from 0.29 to 0.22 when (0.86,1.14) is applied to the neutron scattering from ^{20}Ca.

The isospin dependent Dirac potentials in the *full* density region are determined with the fixed (f_1, f_2). As an example, we present the values for the real and imaginary parts of the Dirac potentials U_s^m and U_0^m for nucleons with an energy of 90 MeV in Fig. 3. The calculated values by DBHF for densities ranging between 0.08 and 0.2 fm^{-3}, as well as those for the auxiliary mesh points are represented by circles, triangles, x marks, and squares for isospin asymmetries $\beta = (\rho_n - \rho_p)/\rho$ of 0.0, 0.2, 0.6, and 1, respectively. The corresponding polynomial interpolations are visualized in terms of a solid line for isospin symmetric nuclear matter ($\beta = 0$), while the dashed line shows the interpolation for the neutron and the dotted line for the proton potentials at $\beta > 0$. It is observed that the microscopic DBHF calculations have almost been rigorously adopted in the present Dirac potentials at $\rho > 0.08$ fm^{-3} and potentials at lower densities decrease, keeping the natural tendency of microscopic calculation, which is good to guarantee the microscopic properties of this MOP. Moreover, U_s^m and U_0^m exhibit a very strong dependence but also a rather smooth way on the neutron-proton asymmetry parameter β at all nuclear densities, as shown in Fig. 3. It is not practical to provide all the fitted polynomial coefficients in this paper to satisfy the diverse applications of the public. We plan to release an executable file on the international web to generate this MOP for any required target and energy automatically in the future.

B. Experimental database

After the optimization by concerning scattering data of ^{40}Ca and ^{208}Pb, the present MOP is assessed through a global prediction and analysis for the main observables of neutron- and proton-induced scattering reactions in a large mass region of $12 \leqslant A \leqslant 209$ below incident energy 200 MeV. The most abundant natural isotopes are considered, and nuclei with even as well as odd mass numbers are incorporated.

TABLE VI. The $d\sigma/d\Omega$ database for proton elastic scattering.

Target	Author (first)	Year	Energy (MeV)	Author (first)	Year	Energy (MeV)
6-C-12	S. Mazzoni	1998	2.5	V. M. Lebedev	2006	7.5
	An-Zhu	2003	22.0	M. Harada	1999	26.0
	M. Ieiri	1987	29.7, 34.5, 44.7	V. I. Grancev	1983	48.5
	A. A. Rush	1971	50.0	M. Ieiri	1987	54.4, 64.9, 74.8, 83.8
	H. O. Meyer	1983	122.0, 160.0, 200.0, 250	V. M. Hannen	2003	150.0
13-Al-27	M. Chiari	2001	0.783, 1,2, 3.01	I. E. Dayton	1956	17.0
	G. M. Crawley	1968	17.5	R. Dittman	1969	28.0
	C. B. Fulmer	1969	61.4	G. Gerstein	1957	92.9, 95.7
	A. E. Taylor	1961	142.0	V. Comparat	1974	156.0
	A. Johansson	1960	160.0, 177.0,183.0	S. Dahlgren	1967	185.0
14-Si-28	E. Fabrici	1980	14.26, 17.24, 20.17, 30.5, 40.21	M. Nakamura	1983	45.0, 50.0, 55.0, 60.0
	S. Kato	1985	65.0	C. Olmer	1984	80.0, 100.0, 135.0, 179.0
	O. Sundberg	1967	185.0	K. H. Hicks	1988	200.0, 250.0
20-Ca-40	J. F. Dicello	1971	10.4, 14.5, 17.6, 20.6	R. H. Mccamis	1986	25.0, 30.0, 35.0, 40.0, 45.0, 48.0
	K. Yagi	1964	55.0	H. Sakaguchi	1982	65.0
	P. Schwandt	1982	80.0, 135.0, 160.0	C. Rolland	1966	152.0
	A. Johansson	1961	182.0	H. Seifert	1993	201.0
26-Fe-56	N. Boukharouba	1992	4.08, 5.02, 6.56, 7.74	K. Kikuchi	1959	7.4, 14.1
	J. Benveniste	1964	10.9	R. Varner	1986	16.0
	I. E. Dayton	1956	17.0	P. Kossanyi-Demay	1967	18.6
	S. F. Eccles	1966	19.1	B. W. Ridley	1964	30.3
	M. K. Brussel	1959	39.8	F. E. Bertrand	1969	61.5
	H. Sakaguchi	1982	65.0	D. J. Steinberg	1964	146
	V. Comparat	1974	156.0	A. Johansson	1961	176
28-Ni-58	L. L. Lee, Jr.	1964	7.0, 8.0, 9.0, 10.0, 11.0, 12.0	S. Kobayashi	1960	14.4, 15.4
	R. Varner	1986	16.0	S. F. Eccles	1966	18.6
	J. R. Tesmer	1972	20.0	E. Fabrici	1980	35.2
	L. N. Blumberg	1966	40.0	C. B. Fulmer	1969	61.4
	H. Sakaguchi	1982	65.0	A. Ingemarsson	1979	178.0
	H. Sakaguchi	1998	192.0	H. Takeda	2003	250.0
40-Zr-90	G. W.Greenlees	1971	9.7	K. Matsuda	1967	14.7
	R. Varner	1986	16.0	J. B. Ball	1964	22.5
	R. De Swiniarski	1977	30.0	L. N. Blumberg	1966	40.0
	C. B. Fulmer	1969	61.4	H. Sakaguchi	1982	65.0
	A. Nadasen	1981	80.0, 135.0, 160.0	V. Comparat	1974	156.0
	E. Hagberg	1971	185.0			
50-Sn-120	G. W. Greenlees	1971	9.7	R. Varner	1986	16.0
	W. Makofske	1972	16.0	S. D. Wassenaar	1989	20.4
	B. W. Ridley	1964	30.3	L. W. Put	1971	30.4
	G. S. Mani	1971	49.4	F. E. Bertrand	1970	61.5
	S. Kailas	1984	104.0	P. Schwandt	1982	135.0
	V. Comparat	1974	156.0	H. Takeda	2003	200.0, 250.0
82-Pb-208	W. Makofske	1972	16.0	W. T. H. Van Oers	1974	21.0, 24.1, 26.3, 30.3, 35.0, 45.0, 47.3
	D. W. Devins	1962	30.8	L. N. Blumberg	1966	40.0
	C. B. Fulmer	1969	61.4	H. Sakaguchi	1982	65.0
	A. Nadasen	1981	80.0, 121.0, 160.0, 182.0	V. Comparat	1974	156.0
	C. Djalali	1982	201.0			

As is well known, the EXFOR library is a comprehensive database that gathers the nuclear reaction measurements of the world [32]. The experimental data adopted in our analysis are all referred in this library. The details of measured elastic scattering angular distribution are specified in this paper by the first author and publication year, which are shown in Tables I and II for neutron-induced reaction and Table VI for proton-incident reaction according to the diversified target nuclei.

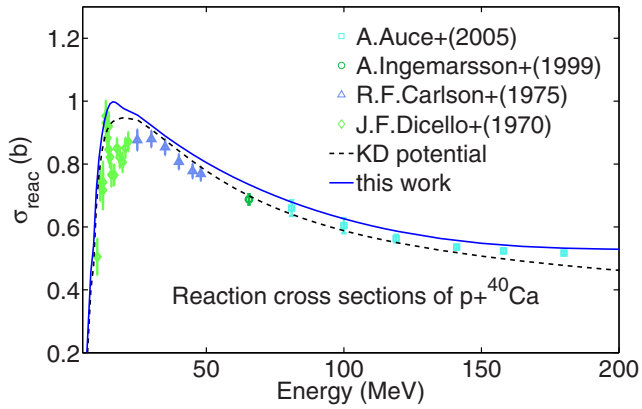

FIG. 16. Comparison of predicted reaction cross section (solid lines) and experimental data (points) and KD calculation (dashed lines) for $p + {}^{40}$Ca.

Other measurements like neutron total cross section and proton reaction cross section are also depicted in the same way in figures.

C. Results for neutron scattering

About 500 sets of elastic scattering angular distributions, 30 sets of analyzing power angular distributions, and 20 sets of total neutron cross sections for 32 different targets are involved in this systematic comparison. The present calculations are compared with experimental data and the results from the widely used KD optical potential.

Because nucleon densities of very light nuclei are not described in a reliable way by means of the Hartree-Fock-Bogoliubov approach, we take ^{12}C as the lightest target in this study. Overall, the predictions of the MOP are in rather good agreement with the experimental data as well as the results calculated by KD potential for such large mass and energy ranges. Meanwhile, it is also observed that the performance of global KD potential is satisfactory even beyond its application scope. The discussion is given in the following sections in detail.

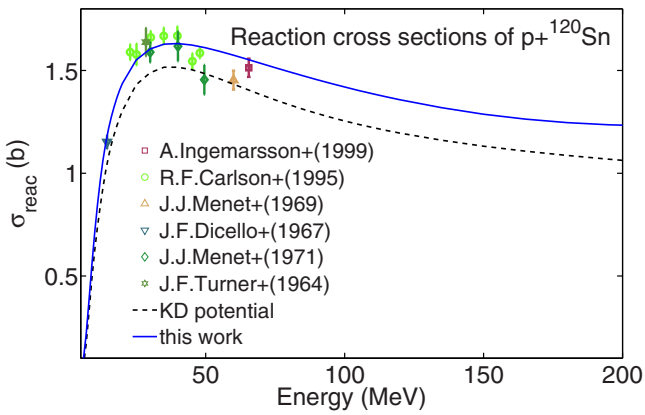

FIG. 17. Comparison of predicted reaction cross section (solid lines) and experimental data (points) and KD calculation (dashed lines) for $p + {}^{120}$Sn.

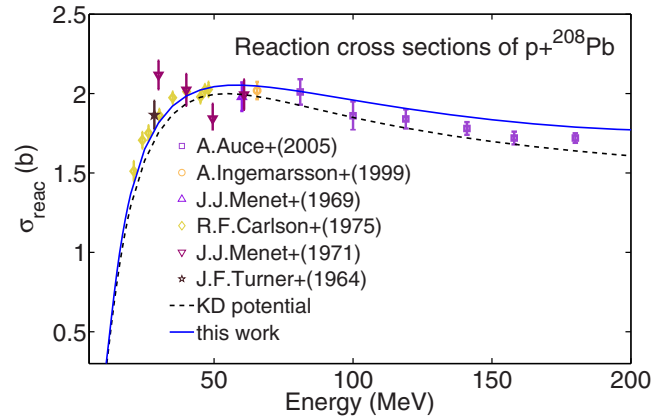

FIG. 18. Comparison of predicted reaction cross section (solid lines) and experimental data (points) and KD calculation (dashed lines) for $p + {}^{208}$Pb.

1. The neutron total cross section

The calculated neutron total cross sections of ^{12}C, ^{56}Fe, and ^{208}Pb are compared with the experimental data and the results of KD potential in Figs. 4, 5, and 6, respectively. Within the scope of application ($E_n > 30$ MeV), a satisfactory prediction is obtained for light nucleus ^{12}C. Because more Ramsauer-like structures appear for the heavy nuclei, the data quality of prediction decreases with increasing mass number. The cross sections are underestimated in this work. The most deviation between experimental data and calculation reaches 10% for ^{208}Pb.

2. The elastic scattering angular distribution

As abundant experimental data exist, we show more concern on $d\sigma/d\Omega$ in this MOP study. Overall, the predicted results are satisfactory even below the energy scope of application of MOP. As the examples, the calculated $d\sigma/d\Omega$ around incident neutron at 30 and 65 MeV are plotted individually in Figs. 7 and 8, where the present predictions coincide with

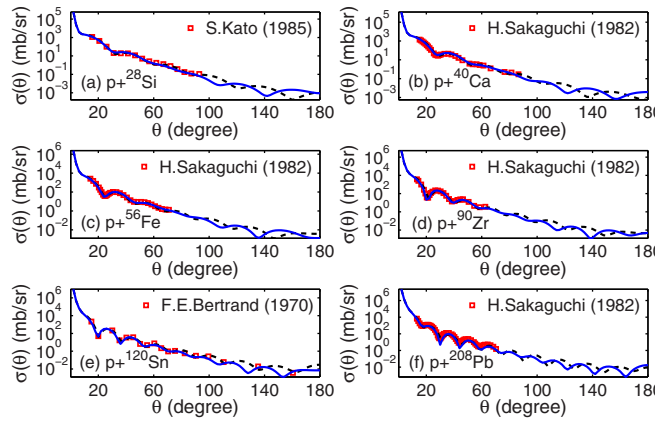

FIG. 19. Comparison of predicted angular distribution (solid lines) and experimental data (points) and KD calculation (dashed lines) for $p + {}^{28}$Si, ^{40}Ca, ^{56}Fe, ^{90}Zr, and ^{208}Pb at incident neutron energy 65 MeV and 61.5 MeV for $p + {}^{120}$Sn.

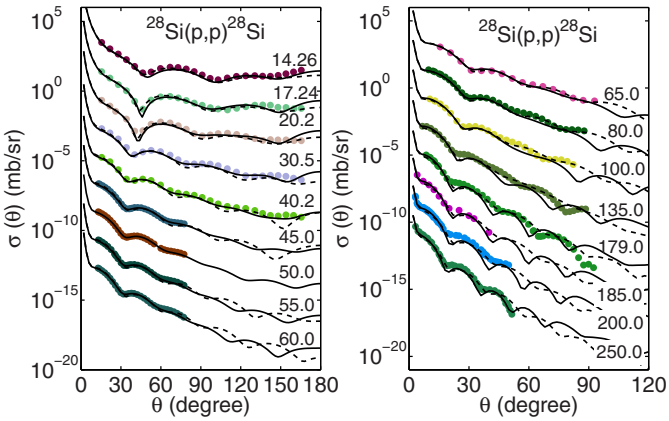

FIG. 20. Comparison of predicted $d\sigma/d\Omega$ (solid lines) and experimental data (points) and KD calculation (dashed lines) for $p + {}^{28}$Si.

experimental data and the KD results very well. More details for diversified nuclei are exhibited in the following contents.

Note that for neutron elastic differential cross sections, as, e.g., in Fig. 9, the incident laboratory energies are in MeV. The curves and data points at the top are true values, while the others are offset by factors of 0.01, 0.0001, etc.

Targets ^{12}C-^{40}Ca. Nine target nuclei including ^{12}C, ^{14}N, ^{16}O, ^{23}Na, ^{24}Mg, ^{27}Al, ^{28}Si, ^{32}S, and ^{40}Ca are examined in this mass region. The results presented in this section are predictions of the present relativistic MOP except that of ^{40}Ca, which is included in the optimization procedure as mentioned in Sec. IV B. The resulting χ^2/N are tabulated in Table III. The results for all nuclei are smaller than 1.0, except for the target nucleus ^{12}C. It is remarkable that the results obtained for the phenomenological KD potential exhibit the same trends as can be observed in the microscopic optical potential. For some target nuclei like, e.g., ^{27}Al both models yield a very small value for χ^2/N, while both models yield a rather poor result for other nuclei, like, e.g., ^{12}C. The scattering on such nuclei is very much influenced by the existence of specific surface excitation modes, which cannot be described in terms of a global optical model (see discussion above). It is worth mentioning that the value for χ^2/N for ^{40}Ca, which has been included in the fit procedure, is comparable to the corresponding value for the other nuclei, which have not been considered in the optimization procedure.

The visual comparisons of the present predictions for ^{12}C, ^{27}Al, and ^{40}Ca with the experimental data, as well as those with KD potential are shown in Figs. 9, 10, and 11, respectively. An excellent agreement with experimental data for $n + {}^{27}$Al is

TABLE VII. The χ^2/N of $d\sigma/d\Omega$ for $p + {}^{12}$C-^{40}Ca reactions.

Nuclide	N of data points	MOP	KD
^{12}C	637	3.70	0.34
^{27}Al	336	0.88	0.90
^{28}Si	513	4.78	0.56
^{40}Ca	682	0.37	0.22

TABLE VIII. The χ^2/N of $d\sigma/d\Omega$ for $p + {}^{56}$Fe-^{208}Pb reactions.

Nuclide	N of data points	MOP	KD
^{56}Fe	516	0.16	0.12
^{58}Ni	557	0.15	0.13
^{90}Zr	536	3.61	0.29
^{120}Sn	406	0.27	0.85
^{208}Pb	1028	0.29	0.72

observed in Fig. 10, as already indicated in the corresponding value for χ^2/N in Table III. From the results displayed in Fig. 9 one can see that main contributions to the large value of χ^2/N for ^{12}C originate from the deviations between measurements and theoretical results at the energies around $E_n = 7$ to 13 MeV. The results for ^{40}Ca by MOP is good except for a slight underestimation at energies 10–20 MeV around the angles between 30° to 60°, while the phenomenological results describe the data in this region in a very reasonable way.

Targets ^{48}Ti-^{63}Cu. We compare results for five nuclei in this mass region, which are important components of structure materials: ^{48}Ti, ^{52}Cr, ^{56}Fe, ^{58}Ni, and ^{63}Cu. The values of χ^2/N are suspended around 0.11–0.17 except for a slightly larger value of 0.23 for ^{56}Fe (see Table IV). As an example we show our prediction for ^{56}Fe in Fig. 12 and compare it with the experimental data and the results of corresponding calculations using the phenomenological KD model. Overall, our results show a fairly good agreement with the experimental data. The largest discrepancies occur for incident energies around 10 to 20 MeV in a region of scattering angles between 30° and 90°. In fact, this deviation appears throughout this mass region.

Targets ^{80}Se-^{209}Bi. Thirteen nuclei including ^{80}Se, ^{88}Sr, ^{89}Y, ^{90}Zr, ^{93}Nb, ^{98}Mo, ^{103}Rh, ^{115}In, ^{120}Sn, ^{140}Ce, ^{197}Au, ^{208}Pb, and ^{209}Bi are utilized to test the performance of this MOP. Good agreement is obtained generally, which could be perceived through the criteria χ^2/N in Table V and Figs. 13 and 14 for ^{98}Mo, ^{103}Rh, and ^{208}Pb. It is noticed that the deviation in the minimum of the angular distribution at scattering angels 30°–60° around $E_n = 20$ MeV, which has been discussed above for ^{48}Ti-^{63}Cu, also shows up for these nuclei. The results near the incident energy 20–30 MeV generally exhibit the underestimation around 50°, which is illustrated also by $d\sigma/d\Omega$ for ^{208}Pb in Fig. 14. Apart from these defects above, all the $d\sigma/d\Omega$ for other heavy target nuclei are reproduced in a very nice way.

3. *The analyzing power*

As mentioned above, it is an important feature of the relativistic description that the spin-orbit term can be naturally involved in the scheme without any additional parameter, which is beneficial to derive the spin-orbit observables $A_y(\theta)$ and $Q_y(\theta)$. The $A_y(\theta)$ at incident energies around 10 MeV are selected to show the ability of predictions for ^{12}C, ^{40}Ca, ^{58}Ni, and ^{208}Pb in Fig. 15, and good agreements with the experimental data for all nuclei are obtained.

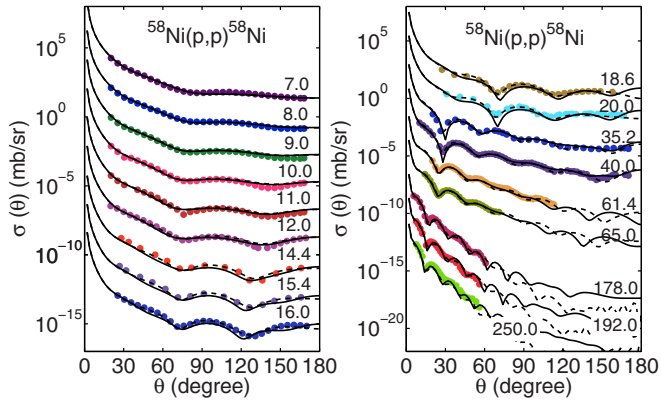

FIG. 21. Comparison of predicted $d\sigma/d\Omega$ (solid lines) and experimental data (points) and KD calculation (dashed lines) for $p + {}^{58}$Ni.

D. Results for proton scattering

About 150 elastic scattering angular distributions, 65 analyzing powers, and reaction cross sections of ten commonly targets have been included in our systematic comparison. The experimental database of $d\sigma/d\Omega$ is summarized in Table VI and depicted by the first author there. As for other quantities, the experimental data for plotting are introduced in the figures.

We compare the present calculations with the experimental data and KD results. As a whole, the various proton scattering observables are predicted satisfactorily using MOP just like its performance in neutron scattering reactions; the results are discussed in the following sections.

1. The proton reaction cross section

It is noticed that the experimental data of proton reaction cross sections, $\sigma_{\rm reac}$, are much less than $\sigma_{\rm tot}$ for neutron in both quantity and in quality. Therefore, we also refer to the calculated $\sigma_{\rm reac}$ by KD potential in the process of visual goodness-of-fit estimation. We sample the predicted $\sigma_{\rm reac}$ for ^{40}Ca, ^{120}Sn, and ^{208}Pb in Figs. 16, 17, and 18. It can be observed that the present calculations are good but only slightly overestimate the experimental values in the whole energy region. In some cases, such as $p + {}^{120}$Sn in the lower energy region, this MOP looks better than the global KD. After comparisons, the maximum deviation between the predicted reaction cross sections and measurements is less than 20%.

2. The elastic scattering angular distribution

We collect the proton elastic scattering angular distribution just as the case for neutron. The $d\sigma/d\Omega$ of proton scattering from six nuclei, ^{28}Si, ^{40}Ca, ^{56}Fe, ^{90}Zr, ^{120}Sn, and ^{208}Pb, around proton incident energy at 65 MeV are collected in Fig. 19. The perfect agreement between the present calculations and experimental data displays the powerful prediction ability of this MOP. In addition, we also condense $d\sigma/d\Omega$ curves of various energies belonging to the same nucleus in one figure, as in Fig. 20. Similarly, in these condensed figures, the curves and data points at the top are true values, while the others are offset by factors of 0.01, 0.0001, etc., and incident laboratory energies are in MeV.

Targets ^{12}C -^{40}Ca. With respect to the differential cross section $d\sigma/d\Omega$, the resulting χ^2/N of nuclei in this mass region are listed in Table VII. The values for ^{12}C and ^{28}Si are obviously larger than for the other nuclei. To explore the source of this discrepancy, we focus our discussion on ^{28}Si (see Fig. 20). It is observed that the theoretical results and the measurements are in good agreement within the entire angular region for incident energies $E_p < 120$ MeV. At higher energies, however, our predictions tend to underestimate the data for the differential cross section. This feature is the main resources to cause the poor χ^2/N.

Targets ^{48}Ti -^{208}Pb. The χ^2/N of $d\sigma/d\Omega$ in this target region is shown in Table VIII. The χ^2/N values show a good prediction in this target region. Some of them are even lower than the corresponding values by KD potential. We look through the details by considering $d\sigma/d\Omega$ of ^{58}Ni in Fig. 21. The present predictions, measurements, and phenomenological KD results are consistent perfectly with each other in the entire energy region.

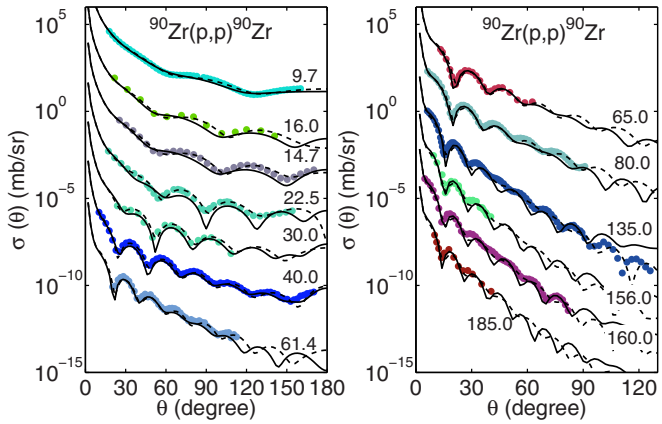

FIG. 22. Comparison of predicted $d\sigma/d\Omega$ (solid lines) and experimental data (points) and KD calculation (dashed lines) for $p + {}^{90}$Zr.

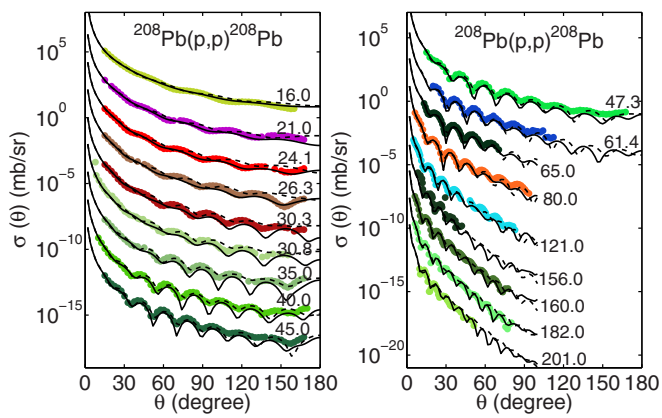

FIG. 23. Comparison of predicted $d\sigma/d\Omega$ (solid lines) and experimental data (points) and KD calculation (dashed lines) for $p + {}^{208}$Pb.

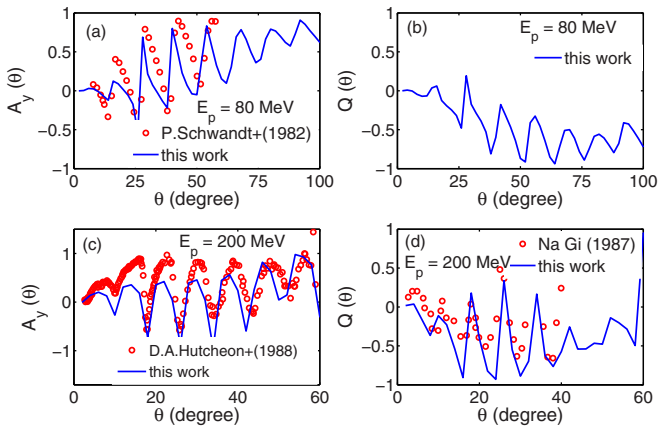

FIG. 24. Comparison of predicted A_y and Q (solid lines) and experimental data (points) for $p + {}^{208}$Pb at $E_p = 80$ and 200 MeV. The experimental data of A_y are taken from the EXFOR library, while the data of Q are read from Ref. [33].

^{90}Zr is the only example for which the χ^2/N is not particularly good. Therefore, we compare the calculated $d\sigma/d\Omega$ for ^{90}Zr in Fig. 22. It is found that most theoretical values are consistent with the measurements, and the main deviations occur at specific incident energies such as 22.5 and 135.0 MeV. In addition, a very good performance of the MOP also occurs in the calculations for $p + {}^{208}$Pb, as shown in Fig. 23.

3. The analyzing power and spin rotation function

The predicted analyzing power $A_y(\theta)$ and spin rotation function $Q(\theta)$ of proton scattering from ^{208}Pb at $E_p = 80$ and 200 MeV are plotted in Fig. 24. The predicted phases of $A_y(\theta)$ and $Q(\theta)$ look well, whereas the amplitudes are not ideal, which remain to be improved in the future. In addition, to show more results of other nuclei, we also plot $A_y(\theta)$ of ^{56}Fe and ^{58}Ni in Fig. 25, where the applied experimental data

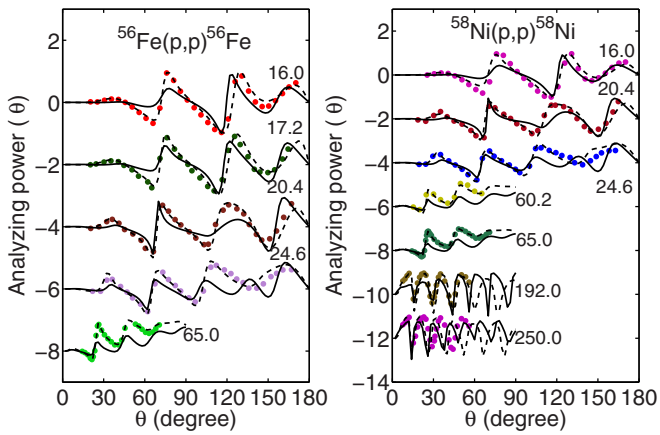

FIG. 25. Comparison of predicted A_y (solid lines) and experimental data (points) and KD calculation (dashed lines) for $p + {}^{56}$Fe and ^{58}Ni. The curves and data points at the top represent true values; the others are offset by factors of 2, 4, 8, etc.

TABLE IX. The A_y database for proton elastic scattering from ^{56}Fe and ^{58}Ni.

Target	Author (first)	Year	Energy (MeV)
26-Fe-56	R. Varner	1986	16.0
	P. J. Van Hall	1977	17.2, 20.4, 24.6
	R. De Leo	1996	65.0
28-Ni-58	R. Varner	1986	16.0
	P. J. Van Hall	1977	20.4, 24.6
	D. C. Kocher	1976	60.2
	H. Sakaguchi	1982	65.0, 192.0
	H. Takeda	2003	250.0

are listed in Table IX. It is shown that the amplitudes of $A_y(\theta)$ by MOP are better around the lower energy region.

V. SUMMARY

The central aim of this study is to provide a relativistic MOP for nucleon-nucleus scattering, which is based on the DBHF calculation of the nucleon self-energy in nuclear matter. After adjustment of very few parameters, the new optical potential qualitatively reproduces many sets of nucleon scattering data for stable targets across the nuclear mass table between ^{12}C to ^{208}Pb at nucleon incident energies below 200 MeV. Therefore, this model can be used to make predictions for unstable targets. At least it can provide an advanced framework for the description of scattering data from unstable nuclei and for studying nuclear structure models of exotic nuclei.

The microscopic basis of this study are Dirac-Brueckner-Hartree-Fock calculations of nuclear matter using realistic forces, which have been adjusted to describe nucleon-nucleon scattering phases. One of the basic features of this relativistic approach is that it provides a specific energy dependence for the optical model and also predicts a spin-orbit term without the need to introduce any additional parameters (see, e.g., Ref. [18]).

The complex isospin dependent self-energies are extracted from the DBHF approach with projection techniques using the Bonn B bare NN interaction. The MOP with Bonn A has also been tested and the results show that the prediction of the scattering for finite nuclei is not very sensitive to the choice of a realistic nucleon force, Bonn A or Bonn B. Therefore, Bonn B has been adopted following our pilot study [17]. The present MOP is very strictly built on the DBHF calculations in nuclear matter at $\rho > 0.08\,\mathrm{fm}^{-3}$ by means of the improved local density approximation. For the purpose of describing the observables of scattering, we construct the optimization method according to the annealing algorithm. The range factors in ILDA and the scalar and vector potentials below 0.08 fm^{-3} are extracted using this method from the experimental data of ^{40}Ca as an example for isospin symmetric nuclei and ^{208}Pb for isospin asymmetric nuclei. Then they are applied for many nuclei and energy regions. Good predictions for most nuclei are achieved by the resulting MOP only with the free parameter t. The results of the MOP are of a quality, which is comparable to the widely used phenomenological KD

global potential. A bit of imperfection still exists in both $n + A$ and $p + A$ systems for specific target nuclei.

Certainly, it is impossible to depict all quantities in a perfect way within the spherical nuclear optical model and the present MOP, especially for the strongly deformed nuclei around rare earth and actinide. Also, it should be kept in mind that the MOP is based on a microscopic study of nuclear matter. Therefore, all features, which are related to surface excitation, e.g., the particle-vibration coupling, are not explicitly taken into account. Such features shall be included in future studies. Moreover, we plan to make the present MOP available in the form of an interactive web-based application.

ACKNOWLEDGMENTS

We thank Professor S. Hilaire for kindly supplying us all the density distributions of finite nuclei calculated in the Hartree-Fock-Bogoliubov (HFB) approach with Gogny D1S force. R. R. Xu thanks Professor Q. B. Shen and Y. L. Han for helpful discussion on the code APMN and physics. This work has been supported by the National Basic Research Program of China under Grant No. 2013CB834404 and the National Natural Science Foundation of China (Grants No. 11305270 and No. 11275018); the Deutsche Forschungsgemeinschaft (DFG) under Contract No. Mu 705/10-1.

[1] M. T. Pigni, M. Herman, P. Obložinský, and F. S. Dietrich, Phys. Rev. C **83**, 024601 (2011).
[2] G. Blanchon, M. Dupuis, H. F. Arellano, and N. Vinh Mau, Phys. Rev. C **91**, 014612 (2015).
[3] L. G. Cao, G. Colo, H. Sagawa, and P. F. Bortignon, Phys. Rev. C **89**, 044314 (2014).
[4] L. Ray, G. W. Hoffmann, and W. R. Coker, Phys. Rep. **212**, 223 (1992).
[5] J. P. Jeukenne, A. Lejeune, and C. Mahaux, Phys. Rev. C **16**, 80 (1977).
[6] Y. L. Xu, H. R. Guo, Y. L. Han, and Q. B. Shen, J. Phys. G **41**, 015101 (2014).
[7] K. Amos, P. J. Dortmans, H. V. von Geramb, S. Karataglidis, and J. Raynal, Adv. Nucl. Phys. **25**, 1 (2000).
[8] P. J. Dortmans, K. Amos, S. Karataglidis, and J. Raynal, Phys. Rev. C **58**, 2249 (1998).
[9] P. K. Deb, K. Amos, S. Karataglidis, M. B. Chadwick, and D. G. Madland, Phys. Rev. Lett. **86**, 3248 (2001).
[10] B. A. Brown, Phys. Rev. Lett. **85**, 5296 (2000).
[11] P. K. Deb, B. C. Clark, S. Hama, K. Amos, S. Karataglidis, and E. D. Cooper, Phys. Rev. C **72**, 014608 (2005).
[12] A. Lagoyannis, Phys. Lett. B **518**, 27 (2001).
[13] M. Dupuis, S. Karataglidis, E. Bauge, J. P. Delaroche, and D. Gogny, Phys. Rev. C **73**, 014605 (2006).
[14] M. Dupuis, S. Karataglidis, E. Bauge, and J. P. Delaroche, Phys. Lett. B **665**, 152 (2008).
[15] K. Amos, P. J. Dortmans, H. V. von Geramb, S. Karataglidis, and J. Raynal, Adv. Nucl. Phys. **25**, 276 (2000).
[16] E. D. Cooper, S. Hama, B. C. Clark, and R. L. Mercer, Phys. Rev. C **47**, 297 (1993).
[17] R. R. Xu, Z. Y. Ma, E. N. E. van Dalen, and H. Müther, Phys. Rev. C **85**, 034613 (2012).
[18] E. N. E. van Dalen and H. Müther, Int. J. Mod. Phys. E **19**, 2077 (2010).
[19] A. H. Lippok and H. Müther, Phys. Rev. C **92**, 034312 (2015).
[20] Z. H. Li, U. Lombardo, H. J. Schulze, and W. Zuo, Phys. Rev. C **77**, 034316 (2008).
[21] E. N. E. van Dalen, C. Fuchs, and A. Faessler, Nucl. Phys. A **744**, 227 (2004).
[22] A. J. Koning and J. P. Delaroche, Nucl. Phys. A **713**, 231 (2003).
[23] T. Gross-Boelting, C. Fuchs, and Amand Faessler, Nucl. Phys. A **648**, 105 (1999).
[24] Z. Y. Ma, P. Zhu, Y. Q. Gu, and Y. Z. Zhou, Nucl. Phys. A **490**, 619 (1988).
[25] E. N. E. van Dalen, C. Fuchs, and A. Faessler, Eur. Phys. J. A **31**, 29 (2007).
[26] E. N. E. van Dalen and H. Müther, Phys. Rev. C **82**, 014319 (2010).
[27] R. Machleidt, K. Holinde, and Ch. Elster, Phys. Rep. **149**, 1 (1987).
[28] S. Hilaire and M. Girod, Eur. Phys. J. A **33**, 237 (2007).
[29] J. W. Negele, Phys. Rev. C **1**, 1260 (1970).
[30] Q. B. Shen, Nucl. Sci. Eng. **141**, 78 (2002).
[31] F. G. Perey, Phys. Rev. **131**, 745 (1963).
[32] https://www-nds.iaea.org/exfor/exfor.htm; V. McLane, BNL-NCS-63380-2000/05-Rev 2000.
[33] Ch. Elster and S. P. Weppner, Phys. Rev. C **57**, 189 (1998), and the reference therein.